SUPPLEMENTARY INFORMATION

SUPPLEMENTARY FOOTNOTES

Footnote S1. Amplitude of gravity-induced receiver deflections. It has not been known whether the antennal receiver may really be deflected by gravity. The gravitational force imposed on objects near the earth's surface is $F = m\ddot{X}$, where m is the mass of the object and $\ddot{X}$ is the acceleration due to gravity (ca. 9.8 m/s^2). The apparent mass of the fly's antennal receiver is ca. $5 \cdot 10^{-12}$ kg, as judged from the free fluctuations of the arista-tip[1], so the force gravity imposes is ca. 50 pN. Because the steady-state stiffness $K_{steady} = F / X$ of the arista-tip is ca. 50 μN/m (See Albert *et al.*[2]), gravity will displace the arista-tip by a distance X of ca. 1μm. This displacement amplitude evoked calcium-signals (Supplementary Fig. S3a) and seems well within the dynamic range of the subgroup-CDE JO neurons' response, which spans arista-tip displacements between ca. 0.1 and 4 μm (Fig. 4e, JO-B + JO-AB > *ricin toxin* flies).

Footnote S2. Stimulus amplitude and receiver vibrations. The pulse songs of courting males reach particle velocities of up to ca. 2.8 mm/s (95 dB)[3]. Following a previous report[4], we presented the songs at pressure amplitudes of up to ca. 100 dB, which, under far-field conditions, corresponds to particle velocities of up to ca. 5 mm/s. This latter particle velocity will displace the arista-tip by ca. 1 μm (See Göpfert *et al.*[5]).

Footnote S3. Hyperpolarisation of JO neurons. We found that JO neurons are not only activated (depolarised) when stretched but are also deactivated (hyperpolarised) when compressed. This deactivation is consistent with the correlations of transducer gating in the antennal receiver's mechanics[2], which suggests that the stationary open probability of the transducer channels in JO neurons is ca. 0.5. Accordingly, deflecting the receiver forwards increase the transducer open probability in the JO neurons of the anterior region while reducing the probability in the posterior region. Together, auditory anatomy and transducer characteristics suffice to account for the opposing calcium signals observed in response to static receiver deflections.

Footnote S4. Distribution of the flies in the counter-current apparatus. In the negative gravitaxis assay, flies were distributed into six tubes by being asked five times to climb up or to stay (Fig. 3a). If the population of the flies is genetically homogeneous and if each fly acts independently and has a constant probability of climbing up in all trials, the final distribution of the flies is expected to match a binomial distribution[6]. By comparing measured distributions to binomial distributions with the measured partition coefficient Cf (the probability of fly's climbing at each trial), we confirmed that the distribution of intact wild-type flies and flies with ablated aristae can be regarded as binomial ($p < 0.05$, Fisher's exact test). We thus calculated the partition coefficient Cf as

$$Cf = \frac{\sum_{k=1}^{n} Nk(k-1)}{(n-1)\sum_{k=1}^{n} Nk}$$

where n is the number of tubes (6), and Nk is the number of the flies in the kth tube[6].

Footnote S5. Definition of aberrant gravitaxis. We used two criteria to define abnormal gravitaxis (Fig. 3b, c and Supplementary Fig. S4b). First, statistically significant changes in negative gravitaxis were determined from the differences in the partition coefficient Cf between the four data sets (negative gravitaxis and phototaxis of the flies with and without neuronal silencing, judged by RM-ANOVA and Student's *t*-test). If alterations in negative gravitaxis in flies with selectively silenced JO neurons were due to the general locomotion defects, similar alterations would be observed also in phototaxis behaviour, i.e.,

$$Cf\mathrm{g,c} - Cf\mathrm{g,s} = Cf\mathrm{p,c} - Cf\mathrm{p,s}$$

where $Cf\mathrm{g,c}$, $Cf\mathrm{g,s}$, $Cf\mathrm{p,c}$, and $Cf\mathrm{p,s}$ are the partition coefficients for *negative gravitaxis without silencing* ($Cf\mathrm{g,c}$), *negative gravitaxis with silencing* ($Cf\mathrm{g,s}$), *phototaxis without silencing* ($Cf\mathrm{p,c}$), and *phototaxis with silencing* ($Cf\mathrm{p,s}$), respectively. If the differences between $Cf\mathrm{g,c} - Cf\mathrm{g,s}$ and $Cf\mathrm{p,c} - Cf\mathrm{p,s}$ were not significantly different, they were rejected by RM-ANOVA. On the other hand, if the neural silencing selectively abolishes gravitactic behaviour, changes in gravitaxis will be larger than in phototaxis, i.e.,

$$Cf\mathrm{g,c} - Cf\mathrm{g,s} > Cf\mathrm{p,c} - Cf\mathrm{p,s}$$

Here, the gravitaxis changes will not be rejected by RM-ANOVA. If abnormal gravitaxis was detected by RM-ANOVA ($p < 0.05$), Student's *t*-test was performed between Cf values of control and experimental flies to certify the statistical significance.

Because this criterion does not take into account the absolute Cf value, we set a second criterion. In wild-type controls, most of the flies ended up in the 5th and 6th tubes after the five trials, resulting in high Cf values (0.92 ± 0.04 in negative gravitaxis and 0.90 ± 0.02 in phototaxis, see Fig. 3b and Supplementary Fig. S4a). If flies show impaired gravitaxis and climb or stay randomly (Cf = 0.5), however, most flies will end up in the 3rd and 4th tubes. If the score of the 5th and 6th tubes (right bar in the three-bar chart) was smaller than that of the 3rd and 4th tubes (middle bar in the three-bar chart), flies were judged to behave abnormal. In the ideal binomial distribution, the score of the 3rd and 4th tubes equals that of the 5th and 6th tubes when Cf = 2/3. We therefore regarded the results with Cf < 2/3 as aberrant behaviours. The evaluation based on the first and second criteria matched well for all cases except for JO-all > *tetanus toxin* and JO-AB > *tetanus toxin* (Supplementary Fig. S4b), which displayed general locomotion defects.

Footnote S6. Higher-order neurons innervating the AMMC. We were able to confirm that higher-order neurons AMMC-A1 and AMMC-B2, the giant fibre neuron (GFN), and the AMMC-CE1 arborise exactly in the same area as the terminals of JO neurons, because the lines used for visualising these neurons label both higher-order neurons and JO neurons. To visualise the arborisations of higher-order neurons selectively, we ablated the antennae of the flies and prepared the brain samples seven days later so that JO neuron-derived GFP signals would not exist in the brain (Fig. 6a left panel, b left panel). For Fig. 6a, left panel, GFP signals of unrelated neurons were erased manually from the confocal section dataset before 3D reconstruction to highlight the morphology of the AMMC-associated neurons.

Footnote S7. Connection between JO neurons and giant fibre neurons. The GFN reportedly receives sensory input from JO neurons[7] and preferentially responds to bimodal stimulation, i.e. vision and mechanical antennal deflection. Because of the difficulty of establishing a behavioural paradigm to test for such bimodal sensory input, whether and how sound stimulation affects the jump response of the flies remains unclear.

Footnote S8. Fly and mammalian sound/gravity sensory systems. In both flies and mammals, sound and gravity are detected by distinct groups of mechanosensory cells. The afferent fibres project through single nerves – antennal nerve (AN) in *Drosophila*[8] and the eighth cranial nerve (N. VIII) in mammals[9,10] – but terminate in spatially segregated primary centres (AMMC zones AB and CE in *Drosophila* and cochlear and vestibular nuclei in mammals[9,10]). Binaural interactions occur between the secondary auditory centres (inferior VLP in *Drosophila* and superior olivary complex as well as inferior colliculus in mammals[9,11]). Apart from the ascending pathway to the secondary centres (cerebellum etc.), the primary centre in the mammalian vestibular pathway has descending pathways directly to the spinal cord, influencing neck motoneurons and ascending proprioceptive afferents[12]. Similarly, the primary gravity centre of the fly (AMMC zone CE) has direct connections to the thoracic ganglia, possibly regulating reflexes as is the case in the mammalian vestibular system[13]. In *Drosophila*, also the auditory pathway has a direct connection to the thoracic ganglia via a single specific neuron, the GFN[14].

Footnote S9. Heterogeneity in the JO neurons. The JO consists of two types of scolopidia that house two and three JO neurons and constitute 90% and 10% of the whole population, respectively[15]. In transgenic flies in which JO neuron subgroups A, B, or CE are selectively labelled, most of the labelled JO neurons seem accompanied by one or two unlabeled neurons[8], suggesting that a single scolopidium can contain JO neurons of different subgroups. Thus, the neurons proper rather than the entire scolopidia seem specialised for detecting gravity and sound.

Subgroups CE of JO neurons respond to both small deflection caused by gravity and large displacements as imposed by air-jets and wind (see accompanying manuscript). Calcium imaging of these neurons showed amplitude-dependent responses with very similar spatial patterns (Supplementary Fig. S3c), suggesting that the neurons that respond to small and large displacements spatially overlap inside JO. The most straightforward interpretation of this observation is that gravity and wind activate the same neurons. Considering the low spatial resolution of the imaging system, however, it is also conceivable that small and large deflections are detected by different sets of JO neurons that are extensively intermingled in the JO array. Because of the limited spatial resolution of the current imaging system and the lack of more specific *GAL4* driver lines to label a smaller subset of subgroups CE neurons, the question of whether the same or different CE neurons respond to gravity and wind remains unsolved.

Footnote S10. Genotypes of experimental flies. Figure 1: F-*GAL4*; UAS-*cameleon2.1-76* (JO-all > *cam2.1*). Figure 2: a, c, d, e, NP1046; UAS-*cameleon2.1-82* (JO-B > *cam2.1*), UAS-*cameleon2.1-82*; JO15/TM6b (JO-AB > *cam2.1*), and NP6250; UAS-*cameleon2.1-76* (JO-CE > *cam2.1*). Figure 3: b, *Canton-S*. c, NP1046/+ (> +) and NP1046/+; tub-*GAL80^{ts}*/+; UAS-*TNT*/+ (JO-B > *tetanus toxin*), NP6250/+ (> +) and NP6250/tub-*GAL80^{ts}*; UAS-*TNT*/+ (JO-CE > *tetanus toxin*), NP6303/+ (> +) and NP6303/tub-*GAL80^{ts}*; UAS-*TNT*/+ (JO-ACE > *tetanus toxin*). Figure 4: b, c, *Canton-S*. d, NP1046/+ (> +) and NP1046/+; tub-*GAL80^{ts}*/+; UAS-*TNT*/+ (JO-B > *tetanus toxin*), NP6250/+ (> +) and NP6250/tub-*GAL80^{ts}*; UAS-*TNT*/+ (JO-CE > *tetanus toxin*), NP6303/+ (> +), and NP6303/tub-*GAL80^{ts}*; UAS-*TNT*/+ (JO-ACE > *tetanus toxin*). e, NP1046/+; ey*FLP*/ UFWTRA19 (JO-B > *ricin toxin*), NP1046/+; NP6250/+; ey*FLP*/UFWTRA19 (JO-B + JO-CE > *ricin toxin*), and NP1046/+; ey*FLP*/+; JO15/UFWTRA19 (JO-B + JO-AB > *ricin toxin*). Figure 5: a, b, F-*GAL4*/UAS > *CD2, y* > *CD8*::*GFP*; ey*FLP*/+ (F-*GAL4* > m*CD8*::*GFP*), and ey*FLP*/UAS > *CD2, y* > *CD8*::*GFP*; nompC-*GAL4.25*/+ (nompC-*GAL4* > m*CD8*::*GFP*). Figure 6: a, NP1046; UAS-*GFP S65T* (T2), NP2802/UAS-*GFP S65T* (T2). b, NP6250/UAS-*GFP S65T* (T2), NP1593/UAS-*GFP S65T* (T2).

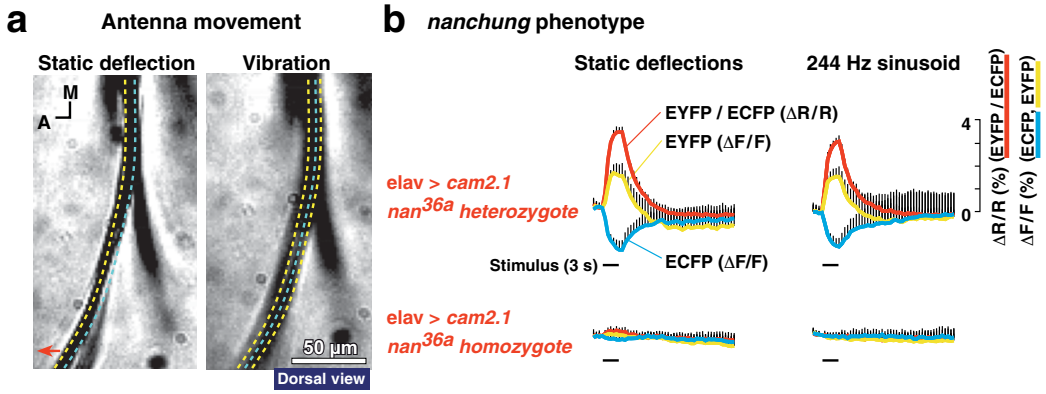

Figure S1 | Movement of the antennal receiver and role of the TRPV channel Nanchung (Nan). a, Tiny movement (~ 5 μm) of the antennal receiver in response to external forcing as seen from the above (yellow) and free fluctuation in the absence of forcing (blue). The stimulus-induced movement was sufficiently large to evoke robust calcium signals in JO neurons. **b,** Reciprocal fluorescent changes (ΔF/F) between ECFP (blue line) and EYFP (yellow line) and the resulting ratio change (ΔR/R, red line) (mean + SD; n = 5 repetitions). Black horizontal bars indicate the stimulus duration (3 s). Mechanically evoked ratio changes were observed in heterozygous control flies of nan^{36a} [16] (Top) but largely reduced in homozygous mutants (Bottom). Interestingly, a small response to static deflection persisted in *nan* mutants, which is consistent with the idea that Nan is not required for transduction but for electrical signal propagation from the site of transduction down to the antennal nerve[5]. Probably, the remnant responses in the mutants are too week to evoke action potentials, as no compound action potentials are detectable in recordings from their antennal nerves[16]. Fly genotypes: $elav^{c155}$-*GAL4*; UAS-*cameleon2.1-76*; nan^{36a}/nan^{36a} (elav > *cam2.1* nan^{36a} *homozygote*), and $elav^{c155}$-*GAL4*; UAS-*cameleon2.1-76*; nan^{36a}/*TM3Ser* (elav > *cam2.1* nan^{36a} *heterozygote*).

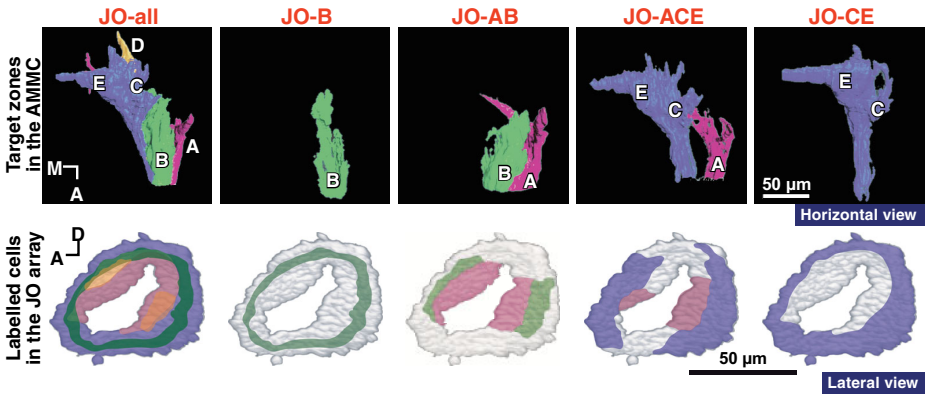

Figure S2 | Distribution of the JO neuron subgroups analysed in this study. The target of JO neurons in the brain – the antennal mechanosensory and motor centre (AMMC) – can be subdivided into five zones (zones A-E; top panels, 3D reconstruction of confocal serial sections with the area of each zone overlaid)[8]. Single-cell labelling and comparison of various *GAL4* driver lines has shown that most JO neurons innervate only a single zone, and that neurons targeting the same zone have their cell bodies in a characteristic area of JO[8]. Each *GAL4* driver line labels various combinations of such subgroups (bottom, schema).

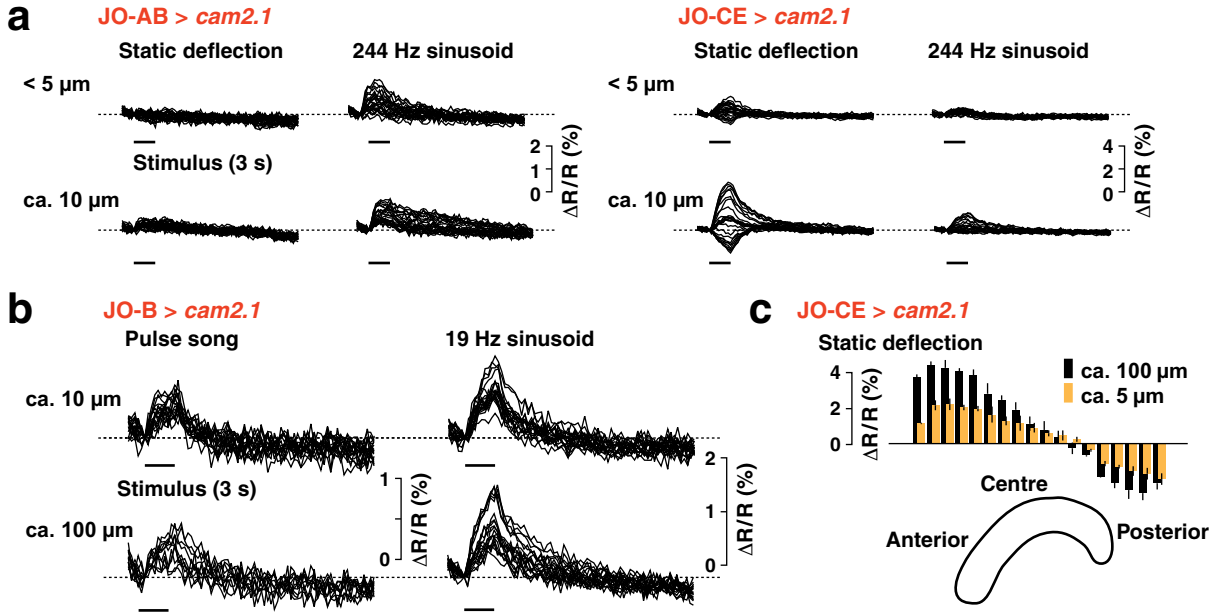

Figure S3 | Responses of JO neuron subgroups AB and CE to mechanical stimuli of varying amplitude. a, Superimposed time traces of ratio changes across the somata array in subgroups AB (left) and CE (right), evoked by small (< 5 μm) and medium (ca. 10 μm) displacement of the arista. Black horizontal bars show stimulus duration (3 s). Dashed horizontal lines indicate zero ratio changes. In subgroups AB, small and medium displacements of the arista evoked ratio changes of similar levels. In subgroups CE, on the other hand, smaller displacements evoked smaller responses, documenting amplitude-dependent calcium signals. **b,** Superimposed time traces of the ratio changes across the JO somata array in vibration-sensitive subgroup B, evoked by medium (10 μm) and very large (100 μm) displacements of the arista. In spite of the different vibration amplitudes, the response amplitude of subgroup B neurons remains largely the same. **c,** Amplitude distribution of the ratio changes in subgroup CE neurons across the somata array (mean ± SD, n = 3 repetition). As in **a**, right panel, calcium signals to small (5 μm, orange bars) and very large (100 μm, black bars) arista displacements increase with the stimulus amplitude. Both stimuli, however, evoke very similar spatial response patterns, suggesting that the neurons producing these responses may be the same. Genotypes: NP1046; UAS-*cameleon2.1-82* (JO-B > *cam2.1*), UAS-*cameleon2.1-82*; JO15/TM6b (JO-AB > *cam2.1*), and NP6250; UAS-*cameleon2.1-76* (JO-CE > *cam2.1*).

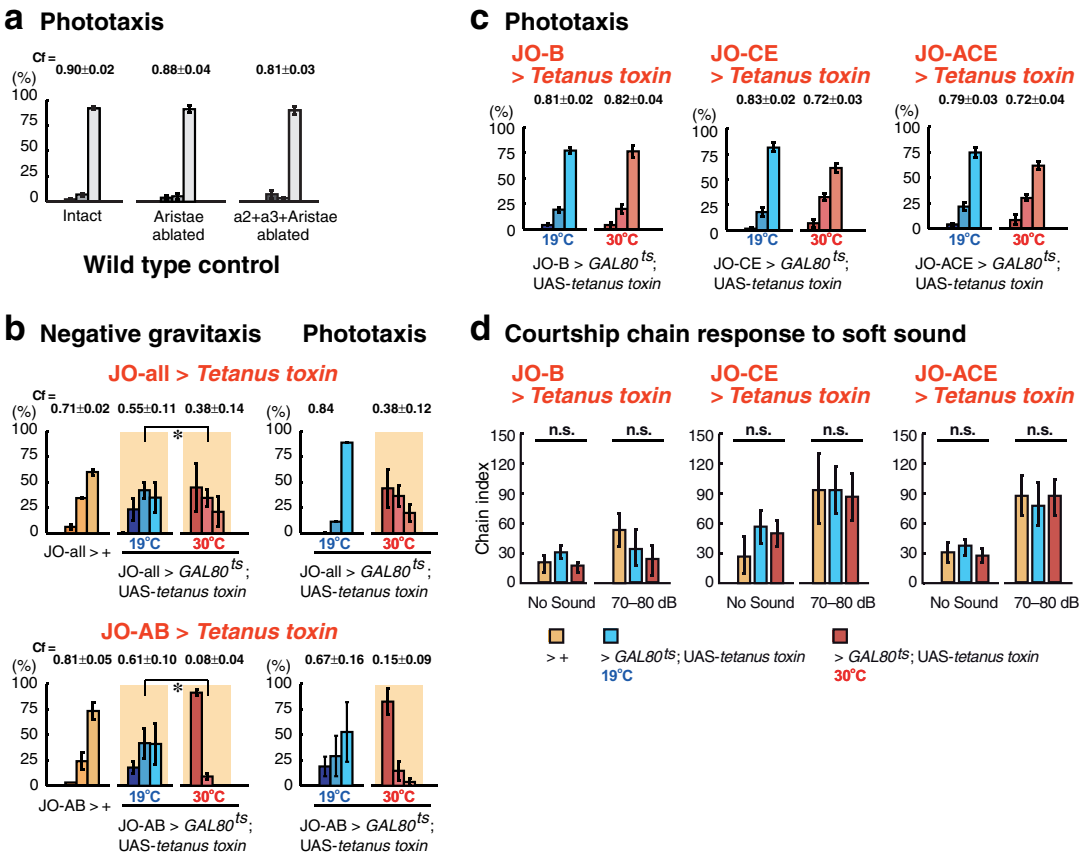

Figure S4 | Negative gravitaxis, phototaxis, and soft sound responses in JO strains. a-c, To assess whether the genetic silencing of JO neuron subgroups selectively abolishes gravitactic behaviour, we measured the phototaxis behaviour under the same experimental condition except for light source placed above the apparatus (mean ± SD; > 4 trials for each experiment except for JO-all > *GAL80^{ts}*; UAS-*tetanus toxin* at the restrictive temperature. *$p < 0.01$; Student's *t*-test calculated after RM-ANOVA. Cases in which the partition coefficient Cf is smaller than 2/3 are highlighted. For statistical analyses, see Supplementary Information footnotes S4, S5). **a,** Phototaxis of flies with ablated antennae. When their antennae were ablated, flies showed significantly lower level of negative gravitaxis (See Fig. 3b) than phototaxis (RM-ANOVA, $p < 0.05$; Student's *t*-test, $p < 0.05$. See Supplementary Information footnote S5). **b,** Aberrant behaviour caused by genetic silencing using *GAL80^{ts}* and UAS-*tetanus toxin*. Silencing all JO neuron subgroups (JO-all) and subgroups AB (JO-AB) abolishes both negative gravitaxis and phototaxis behaviours (the partition coefficients Cf between 0.08 and 0.38), indicating general locomotion defects. **c,** Specific defects in negative gravitaxis. Silencing subgroups B, CE and ACE did not abolish phototaxis (partition coefficients Cf between 0.72 and 0.82). **d,** Courtship chain indices of the flies with genetically silenced JO neurons during stimulation with soft (70-80 dB) sound (mean ± SEM, > 5 trials for each experimental group). JO-B > *Tetanus toxin* flies formed courtship chains less often than controls (1st panel), though this difference is not significant (n.s.: $p > 0.05$, Mann-Whitney U-tests). Silencing subgroups CE and ACE did not significantly alter chaining behaviour, either, suggesting that subgroup A neurons labelled by JO-ACE driver do not play significant roles. This is probably because (1) faint sounds broadcast via a loudspeaker cause particle velocities in the near-field that are still sufficiently large to be detected by flies without subgroup A, (2) the JO-ACE driver does not drive expression of *tetanus toxin* in all subgroup A neurons, and/or, (3) male flies do not require subgroup A-mediated sensitive hearing in this behavioural paradigm. Genotype in a: *Canton-S* (wild type). Genotypes in b: F-*GAL4*/+ (JO-all > +) and F-*GAL4*/tub-*GAL80^{ts}*; UAS-*TNT*/+ (JO-all > *tetanus toxin*), JO15/+ (JO-AB > +) and tub-*GAL80^{ts}*/+; UAS-*TNT*/JO15 (JO-AB > *tetanus toxin*). Genotypes in c: NP1046/+, NP1046/+; tub-*GAL80^{ts}*/+; UAS-*TNT*/+ (JO-B > *tetanus toxin*), NP6250/+, NP6250/tub-*GAL80^{ts}*; UAS-*TNT*/+ (JO-CE > *tetanus toxin*), NP6303/+, NP6303/tub-*GAL80^{ts}*; UAS-*TNT*/+ (JO-ACE > *tetanus toxin*).

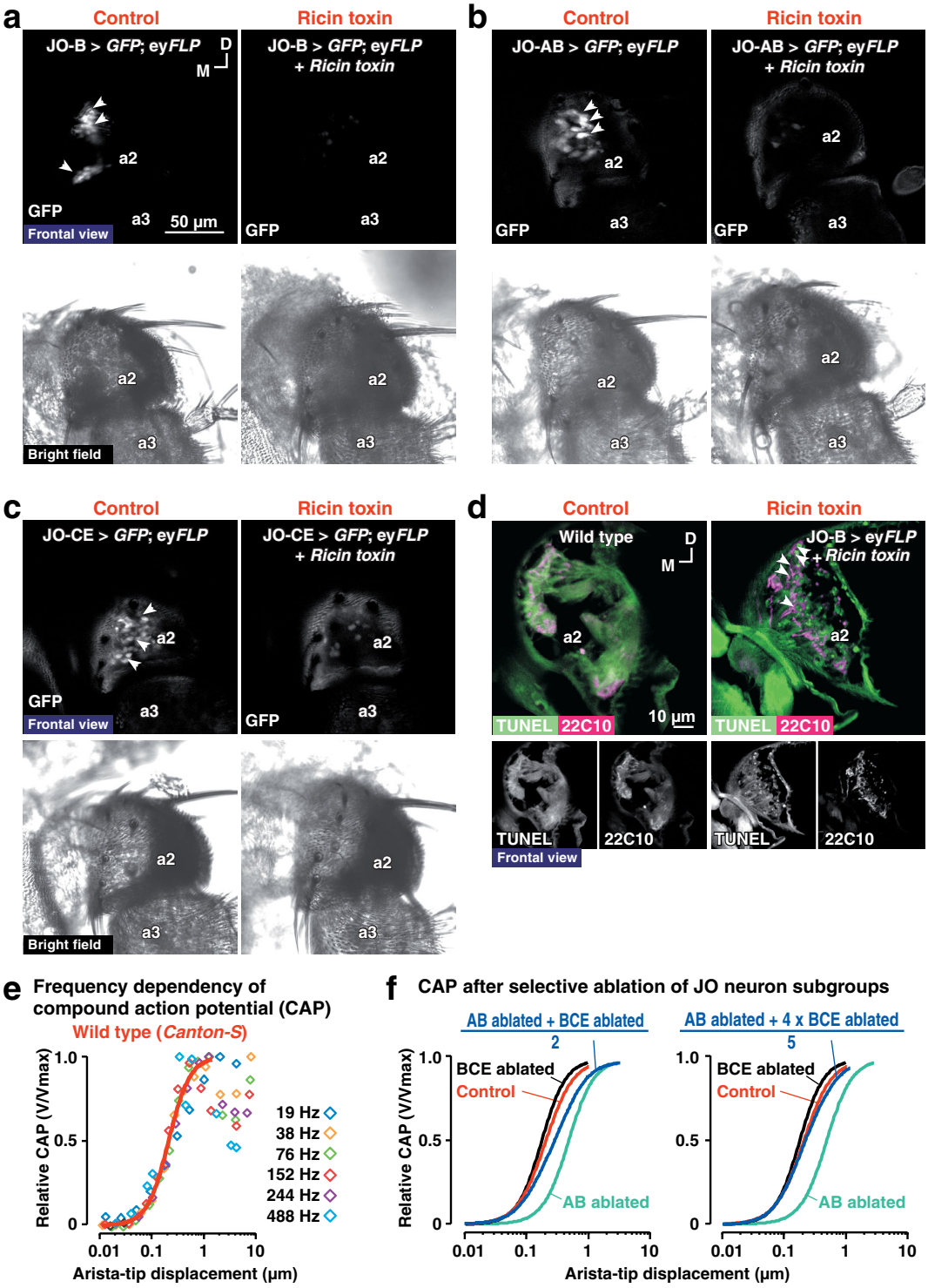
a
Control
Ricin toxin
JO-B > GFP; eyFLP
JO-B > GFP; eyFLP + Ricin toxin
D
M
a2
a3
GFP
Frontal view
50 µm
Bright field
b
JO-AB > GFP; eyFLP
JO-AB > GFP; eyFLP + Ricin toxin
c
JO-CE > GFP; eyFLP
JO-CE > GFP; eyFLP + Ricin toxin
d
Wild type
JO-B > eyFLP + Ricin toxin
TUNEL
22C10
10 µm
Frontal view
e
Frequency dependency of compound action potential (CAP)
Wild type (Canton-S)
Relative CAP (V/Vmax)
1.0
0.5
0
0.01
0.1
1
10
Arista-tip displacement (µm)
19 Hz
38 Hz
76 Hz
152 Hz
244 Hz
488 Hz
f
CAP after selective ablation of JO neuron subgroups
AB ablated + BCE ablated
AB ablated + 4 x BCE ablated
2
5
BCE ablated
Control
AB ablated

Figure S5

Figure S5 | Selective ablation of JO neuron subgroups and compound action potential (CAP) assay in the antennal nerve. a-c, Selective expression of *ricin toxin A chain* abolishes *GFP* expression in JO neurons. Antennae were mounted in 50% glycerol/PBS. Confocal sections were taken with an LSM 510 META laser-scanning microscope (Carl Zeiss). In control flies (left panels), *GFP* is expressed in subgroups of JO neurons (arrowheads). No such GFP signals were observed in the flies expressing both *GFP* and *ricin toxin* (right panels), as is expected for the inhibition of protein synthesis by ricin. Bright-field images of the same samples are shown at the bottom. D, dorsal; M, medial; a2, the second antennal segment; a3, the third antennal segment. **d,** Apoptosis of JO neurons triggered by expression of *ricin toxin*. Heads of newly hatched flies were fixed in 3% paraformaldehyde and embedded in TissueTek (Sakura). Cryosections of 16-μm thickness were subjected to TUNEL staining (green) using the *In Situ* Cell Death Detection Kit, Fluorescein (Roche) according to the protocol provided by the manufacturer. Antibody 22C10 (1:10; Developmental Studies Hybridoma Bank) was used for visualising sensory neurons (magenta). Alexa Fluor 546-conjugated anti-mouse IgG (1:1500; Invitrogen) was used as a secondary antibody. Left: in wild-type control flies, no TUNEL-positive JO neurons are detected. Right: in flies expressing *ricin toxin*, punctate TUNEL-positive signals are seen in JO neurons (arrowheads). **e,** CAP responses of JO neurons of a wild-type fly to pure tones (sinusoidal sound wave) of six different frequencies (19, 38, 76, 152, 244, and 488 Hz). The displacement characteristic of the CAP remained constant when the stimulus frequency was altered, providing a frequency-independent measure of the mechanical sensitivity of JO. **f,** Contribution of different subgroups of JO neurons to the intensity characteristics of the CAP response. Left: If the absolute CAP amplitudes in AB- and BCE-ablated flies were approximately the same, one would expect that the intensity characteristics obtained for these flies (Hill-fits, green and black curves, respectively, same as in Fig. 4e) together sum up to an intensity profile (blue curve) that is clearly different from that of controls (red curve). Right: We found that the absolute peak amplitude of the remnant CAPs in AB-ablated flies is ca. 4 times smaller than that of BCE-ablated flies. (Note that graphs in Fig. 4e and S5e present relative CAP value.) Because of this difference, the intensity curves of AB-ablated and BCE-ablated flies sum up to an intensity profile (blue curve) that closely resembles that observed in controls (red curve). Genotypes in a: NP1046/+; UAS-*GFP S65T*/+; ey*FLP*/TM6b (JO-B > *GFP*; ey*FLP*), and NP1046/+; UAS-*GFP S65T*/+; ey*FLP*/UFWTRA19 (JO-B > *GFP*; ey*FLP*+*ricin toxin*). Genotypes in b: ey*FLP*/UAS-*GFP S65T*; JO15/TM6b (JO-AB > *GFP*; ey*FLP*), and ey*FLP*/UAS-*GFP S65T*; JO15/UFWTRA19 (JO-AB > *GFP*; ey*FLP*+*ricin toxin*). Genotypes in c: NP6250/UAS-*GFP S65T*; ey*FLP*/TM6SbTb (JO-CE > *GFP*; ey*FLP*) and NP6250/UAS-*GFP S65T*; ey*FLP*/UFWTRA19 (JO-CE > *GFP*; ey*FLP*+*ricin toxin*). Genotypes in d: *Canton-S* (wild type), and NP1046/+; ey*FLP*/UFWTRA19 (JO-B > *GFP*; ey*FLP*+*ricin toxin*). Genotype in e: *Canton-S* (wild type). Genotypes in f: NP1046/+; ey*FLP*/+; JO15/UFWTRA19 (AB ablated), NP1046/+; NP6250/+; ey*FLP*/UFWTRA19 (BCE ablated), and *Canton-S* (Control).

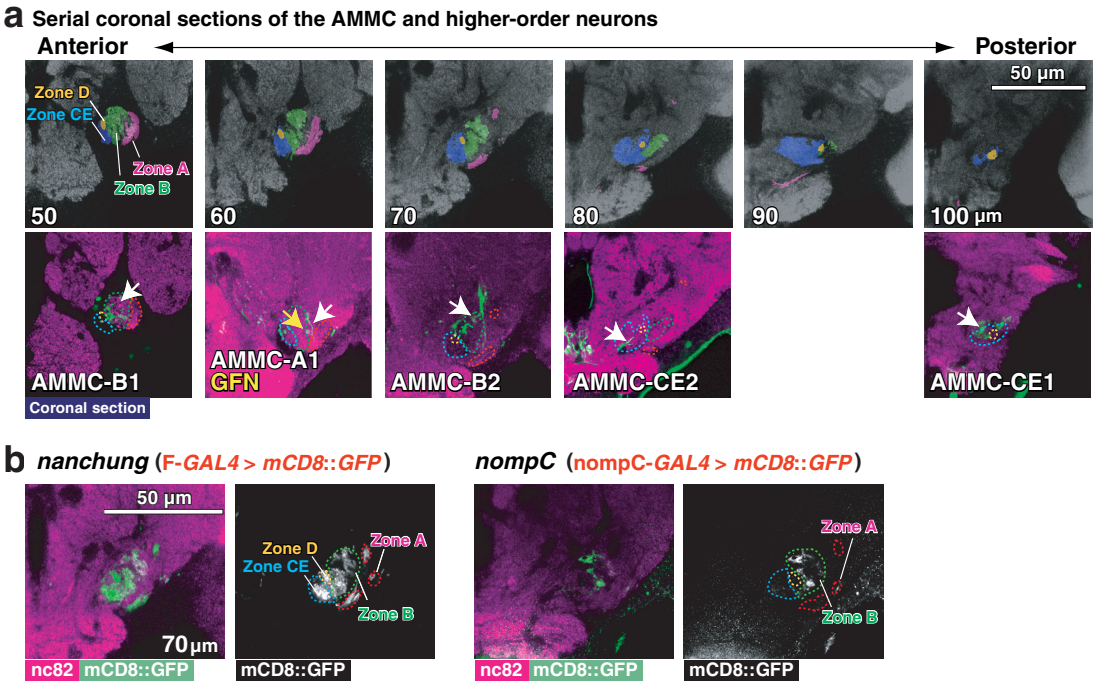

Figure S6 | AMMC zones and the target areas of higher-order neurons. a, Confocal serial optical sections of the brain of a JO-all > *GFP* fly (coronal confocal sections, medial to the left). Top: Zones of the AMMC, colour-coded using AMIRA (Visage Imaging). Zones C and E are not distinguished here as they are more contiguous compared to the other zones[8]. Counterstaining with nc82 antibody is shown in greyscale. Numbers in the lower left indicate the distance of the section (in μm) from the entrance point of the axons of JO neurons in the brain. Bottom: confocal coronal optical sections of the *GAL4* fly strains that label higher-order neurons (see Fig. 6a,b) at the same anteroposterior level as the above sections. Zones (dotted lines) were identified based on the structural features revealed by counterstaining with nc82 (magenta). Arborisations of the higher order neurons (arrows) visualised with *GAL4* driver lines enter the respective zones indicated in Fig. 6a, b. **b,** Confocal optical sections obtained from *GAL4* fly strains that label *nanchung*- and *nompC*-expressing JO neurons. Coronal sections at 70 μm from the entrance point of the axons of JO neurons are shown. Whereas *nanchung* is expressed in JO neurons innervating all zones of the AMMC, *nompC* is expressed only in those neurons that arborise zones A and B. Genotypes in a: 1st and 2nd panels, NP1046; UAS-*GFP S65T* (T2). 3rd panel, NP2802/UAS-*GFP S65T* (T2). 4th panel, NP1593/UAS-*GFP S65T* (T2). 5th panel, NP6250/UAS-*GFP S65T* (T2). Genotype in b: F-*GAL4*/UAS > *CD2, y* > *CD8*::*GFP*; ey*FLP*/+ and ey*FLP*/UAS > *CD2, y* > *CD8*::*GFP*; nompC-*GAL4.25*/+.

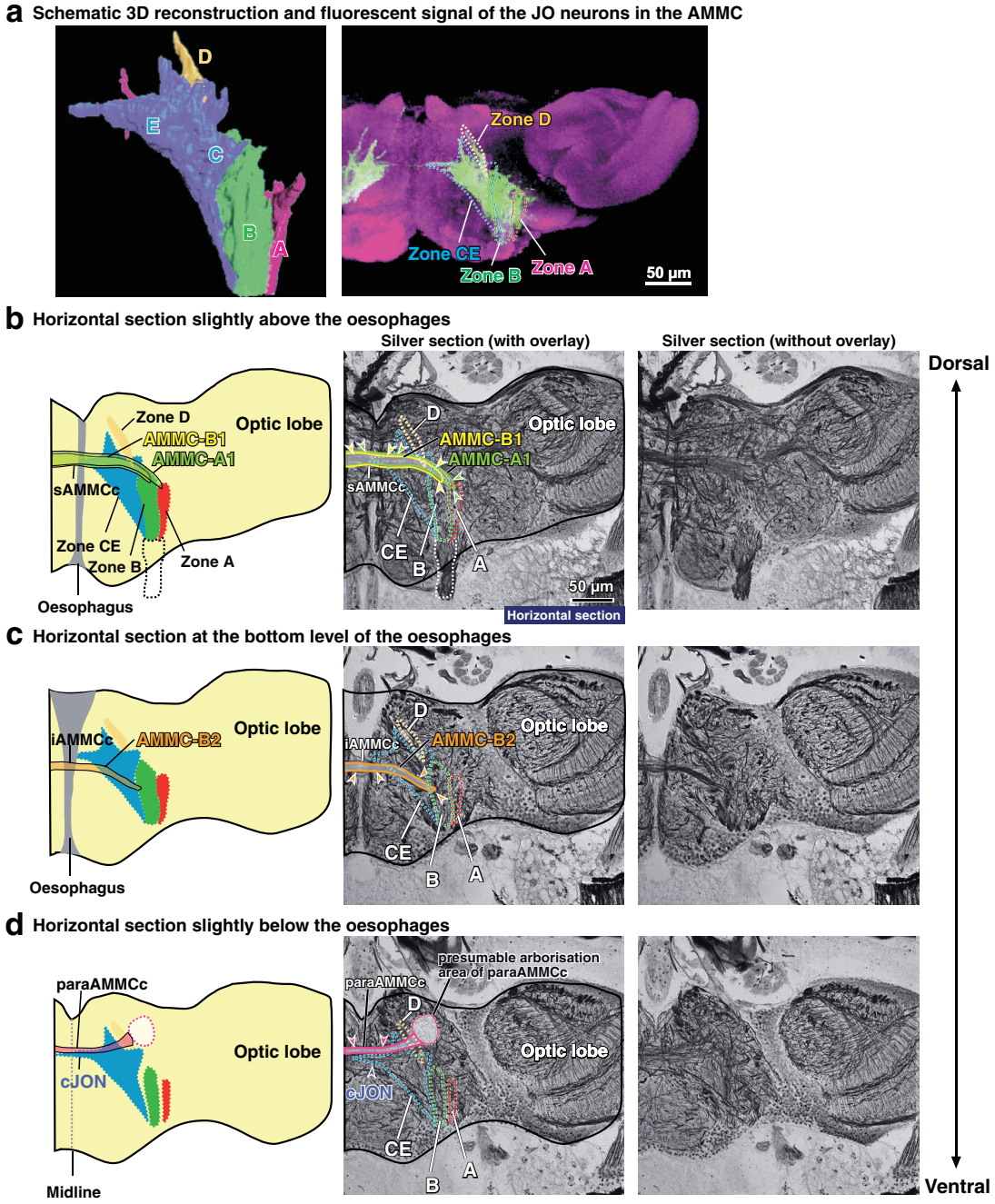

Figure S7 | Commissures connecting AMMC zones. a, Schematic 3D reconstruction (left) and fluorescent signal of the JO neurons in the AMMC (right). White rectangle: the area shown in the sections below. **b-d,** Bodian silver-stained paraffin sections at three dorsoventral levels of the AMMC. Silver staining was performed as described[8]. Left: diagrams of the structures indicated in the sections. Middle: Bodian sections with outlines of zones and commissures. Right: Same sections without overlay. **b,** Section at the level slightly above the oesophagus. Thick commissural bundles of AMMC-A1 and -B1 connect zones A and zones B of both hemispheres, respectively. These neural fibres form a single bundle, the superior AMMC commissure (sAMMCc), which crosses the midline above the oesophagus. **c,** Section at the bottom level of the oesophagus. The thick commissural bundle of AMMC-B2 connects zones B of both hemispheres. At the midline, these neural fibres form the inferior AMMC commissure (iAMMCc) that runs below the oesophagus. **d,** Section at the level slightly below the oesophagus. A small number of axons from JO neurons runs through zones CE and reaches the midline. Though some of these fibres cross the midline via the commissure of JO neurons (cJON), most of them terminate in the area near the midline and seldom reach the core part of the contralateral zones CE[8]. A thin commissure runs just posterior to cJON. Neural fibres of this para AMMC commissure (paraAMMCc) run through zones CE and zone D and arborise in the area posterior lateral to the AMMC (white shaded area with dotted circle). This commissure therefore does not connect the zones CE of both hemispheres.

Supplementary Table S1

Fly strains	N=	f_0, Hz	Q	E, kbT	ΔE, zJ	K_{eff}, μN/m	$\langle X^2 \rangle$, nm²
Experimental							
JO-all > *cam2.1*	5	267±35	1.50±0.34	7.22±1.14	25.6±4.7	2.18±0.91	1087±432
JO-B > *cam2.1*	6	265±36	1.35±0.32	8.74±1.24	31.8±5.1	1.67±0.27	1054±106
JO-AB (hetero) > *cam2.1*	4	250±67	1.10±0.00	5.81±2.21	19.8±9.1	2.97±2.24	928±547
JO-AB (homo) > *cam2.1*	8	307±62	0.88±0.08**	3.41±1.26*	9.9±5.2*	7.28±5.19*	439±237*
JO-CE > *cam2.1*	5	242±29	1.66±0.80	7.93±2.29	28.5±9.4	1.73±0.89	1331±615
Control							
Canton-S	7	253±53	1.39±0.31	8.90±3.05	32.5±12.5	1.94±1.75	1438±748

Table S1 | Principal parameter values of fits of a damped harmonic oscillator model to receiver fluctuations. The performance of the antennal receiver was examined by measuring the free fluctuations of the arista-tip in the absence of external stimulation[1,2]. By fitting the power spectrum of the fluctuations with a simple harmonic oscillator model, the resonance frequency (f_0), the tuning sharpness (quality factor) (Q), the mean total energy (E), the energy contributed by the mechanical activity of JO neurons (ΔE), the effective receiver stiffness (K_{eff}), and the total fluctuation power in the frequency range between 100 and 1500 Hz ($\langle X^2 \rangle$) were determined (for a detailed description, see Göpfert *et al.*[1]). Significant differences (*$p < 0.05$; **$p < 0.01$) from corresponding values of wild-type *Canton-S* flies are shown (Two-tailed Mann-Whitney U-test with the Sidak-Bonferroni correction was used for the determination of significance). In JO-AB > *cam2.1* homozygous flies, the tuning sharpness (quality factor) (Q), the total fluctuation power ($\langle X^2 \rangle$), and the mean total energy (E) of the receiver were significantly lower than in controls. The effective stiffness (K_{eff}) was significantly increased, leading to a drop in the mechanical susceptibility of their receivers. Interestingly, also the neural energy contribution (ΔE) was reduced in these flies, documenting that function of JO neurons is impaired. No significant differences were obtained between other experimental flies (JO-all > *cam2.1*, JO-B > *cam2.1*, JO-AB > *cam2.1* heterozygous flies, and JO-CE > *cam2.1*) and controls. N indicates the number of measured animals.

Supplementary Video 1

This movie shows the spatial activation of the JO somata array (outlined in white line) in a JO-all > *cam2.1* fly to five types of mechanical stimuli: static deflections towards anterior and posterior, pulse song, and 244- and 19-Hz sinusoids. Stimulus duration is indicated by the red square at the top-left (QuickTime; 1.3 MB).

Supplementary Video 2

This movie shows the 3D structure of the zones in the AMMC. Reconstruction was generated from the serial section data shown in Supplementary Video 3 by manually painting the arborisation areas of each zone using Amira 3.1 Software (Visage Imaging) (QuickTime; 4.7 MB).

Supplementary Video 3

This movie shows the serial section of AMMC from the anterior to posterior. The first half of the movie shows the GFP signal (green) in the JO-all > *GFP* fly, counterstained with the nc82 antibody (magenta). In the second half, the labelled areas were painted according to the zone structure of AMMC (QuickTime; 8.9 MB).

Supplementary Video 4

This movie shows the counter-current apparatus in action. Actual experiments were performed in pitch darkness. Under bright light condition, flies show both negative-gravitaxis and phototaxis, leading to a high partition coefficient Cf. Note that some parts of the movie are played at 10x speed (QuickTime; 4.2 MB).

Supplementary Video 5

This movie shows the response of the flies to a synthesized courtship pulse song. The left and right chambers house flies with intact and ablated antennae, respectively. Behaviours observed in the absence of sound and the presence of mild and loud sounds are shown. Excerpt from 10-min recording (QuickTime; 7.9 MB).

SUPPLEMENTARY METHODS

Equipment and settings. For calcium imaging analysis (Figs 1, 2, and Supplementary Figs S1 and S3), a cameleon 2-filter set (455 nm DCLP, 515 nm DCLP, 535/30 nm emission filter, 485/40 nm emission filter; part #71007, Chroma Technology) and a beam-splitter device Dual View (Photometrics) were used for detecting the EYFP and ECFP images simultaneously with a single CCD chip. Pseudocolour images were constructed using a Pseudocolour lookup table available in MetaMorph software (Molecular Devices). Contrast of digital images was adjusted with Photoshop CS software (Adobe Systems). For confocal images (Figs 1b, 2b, 5, 6, and Supplementary Figs S2, S5a-d, S6, and S7a), serial optical sections at 0.5-1.2 μm intervals were taken with LSM 510 confocal microscopes (Carl Zeiss) equipped with a water-immersion 40x Plan-Apochromat objective (NA = 1.2; Figs 1b, 2b, 5b, and Supplementary Figs S2 and S7a) and a 63x Plan-Apochromat objective (NA = 1.2; Fig. 6a, b, and Supplementary Fig. S6), with an LSM 510 META confocal microscope (Carl Zeiss) equipped with a 20x Plan-Apochromat objective (NA = 0.75; Supplementary Fig. S5a-d), and with a FV1000 confocal microscope (Olympus) equipped with an oil-immersion 60x UPLSAPO objective (NA = 1.35; Fig. 5a). Confocal datasets were processed with 3D-reconstruction software Volocity 3.0 (Improvision; Fig 1b), Amira 3.1 (Visage Imaging; Fig. 2b and Supplementary Figs S2 and S7a), and Imaris 2.7 (Bitplane AG; Fig. 6a, b). GFP, Alexa Fluor 488-conjugated goat anti-rabbit IgG, and TUNEL signals were excited at 488 nm and detected via a 500–540 nm band-pass filter. Alexa Fluor 546-conjugated anti-mouse IgG (Supplementary Fig. S5d) was excited at 543 nm and detected via a 560-615 nm band-pass filter. Alexa Flour 633-conjugated goat anti-mouse IgG signal (Figs 2b, 5b and Supplementary Figs S6 and S7a) was excited at 633 nm and detected via a 650 nm long-pass filter. The resolution of a single confocal section was 1024 x 1024 pixels (Figs 6a, b, and Supplementary Figs S2, S5 and S6) and 512 x 512 pixels (Figs 1b, 2b, 5 and Supplementary Fig. S7a). For Fig 2b and Supplementary Figs S2, S6 and S7a, images of serial confocal sections were painted manually using Amira 3.1 software (Visage Imaging) to show the arborisation areas of each zone. For visualising the morphology of individual neurons in Fig. 6, signals of other labelled cells were erased manually from the confocal data set[17]. To do this, a series of TIFF-format confocal images was imported to ImageReady software (Adobe Systems) and, by comparing the neighbouring sections, signals attributed to other labelled cells were painted in background colour. For silver-stained sections (Supplementary Fig. S7b-d), images were taken with a 40x Plan-Apochromat objective lens (n.a. 1.3) with Nomarski optics using an Axioplan microscope (Carl Zeiss) and an AxioCam HRc digital camera (Carl Zeiss). For each 7-μm paraffin section, a series of 3 images of 2560 x 2048 pixels were taken at slightly different focal planes and overlaid using Image-J (NIH) with StackReg and Stack Focuser plug-ins to achieve broader depth of focus. The size, contrast, and brightness of the resulting images were adjusted with Photoshop CS software (Adobe Systems).

REFERENCES FOR SUPPLEMENTARY INFORMATON

1. Göpfert, M.C., Humphris, A.D., Albert, J.T., Robert, D. & Hendrich, O. Power gain exhibited by motile mechanosensory neurons in *Drosophila* ears. *Proc. Natl. Acad. Sci. USA* **102**, 325-330 (2005).
2. Albert, J.T., Nadrowski, B. & Göpfert, M.C. Mechanical signatures of transducer gating in the *Drosophila* ear. *Curr. Biol.* **17**, 1000-1006 (2007).
3. Bennet-Clark, H.C. Acoustics of insect song. *Nature* **234**, 255-259 (1971).
4. Eberl, D.F., Duyk, G.M. & Perrimon, N. A genetic screen for mutations that disrupt an auditory response in *Drosophila melanogaster*. *Proc. Natl. Acad. Sci. USA* **94**, 14837-14842 (1997).
5. Göpfert, M.C., Albert, J.T., Nadrowski, B. & Kamikouchi, A. Specification of auditory sensitivity by *Drosophila* TRP channels. *Nat. Neurosci.* **9**, 999-1000 (2006).
6. Benzer, S. Behavioral mutants of *Drosophila* isolated by countercurrent distribution. *Proc. Natl. Acad. Sci. USA* **58**, 1112-1119 (1967).
7. Bacon, J.P. & Strausfeld, N.J. The dipteran 'Giant fibre' pathway: neurons and signals. *J. Comp. Physiol. A* **158**, 529-548 (1986).
8. Kamikouchi, A., Shimada, T. & Ito, K. Comprehensive classification of the auditory sensory projections in the brain of the fruit fly Drosophila melanogaster. *J. Comp. Neurol.* **499**, 317-356 (2006).
9. Hudspeth, A.J. *Hearing*: in *Principles of Neural Science* (eds Kandel, E.R., Schwartz, J.H. & Thomas, M.J.) 590-613 (McGraw-Hill, New York, 2000).
10. Goldberg, M.E. & Hudspeth, A.J. *The Vestibular System*: in *Principles of Neural Science* (eds Kandel, E.R., Schwartz, J.H. & Thomas, M.J.) 801-815 (McGraw-Hill, New York, 2000).
11. Cant, N.B. & Benson, C.G. Parallel auditory pathways: projection patterns of the different neuronal populations in the dorsal and ventral cochlear nuclei. *Brain. Res. Bull.* **60**, 457-474 (2003).
12. Büttner-Ennever, J.A. A review of otolith pathways to brainstem and cerebellum. *Ann. N. Y. Acad. Sci.* **871**, 51-64 (1999).
13. Barmack, N.H. Central vestibular system: vestibular nuclei and posterior cerebellum. *Brain. Res. Bull.* **60**, 511-541 (2003).
14. Phelan, P. *et al.* Mutations in *shaking-B* prevent electrical synapse formation in the *Drosophila* giant fiber system. *J. Neurosci.* **16**, 1101-1113 (1996).
15. Todi, S.V., Sharma, Y. & Eberl, D.F. Anatomical and molecular design of the *Drosophila* antenna as a flagellar auditory organ. *Microsc. Res. Tech.* **63,** 388-389 (2004).
16. Kim, J. *et al.* A TRPV family ion channel required for hearing in *Drosophila*. *Nature* **424**, 81-84 (2003).
17. Otsuna, H. & Ito, K. Systematic analysis of the visual projection neurons of *Drosophila melanogaster.* I. Lobula-specific pathways. *J. Comp. Neurol.* **497**, 928-958 (2006).